Article

Changes in marine sedimentation patterns in the northeastern South China Sea in the past 35,000 years

Check for updates

Kuan-Ting Chen[1], Shu-Kun Hsu [1,2 ✉], Andrew Tien-Shun Lin[1], Chih-Chieh Su [3], Nathalie Babonneau[4], Gueorgui Ratzov[5], Serge Lallemand[6], Pi-Chun Huang[1], Lien-Kai Lin[1], Hsiao-Shan Lin[7], Ching-Hui Tsai[7], Jing-Yi Lin[1] & Song-Chuen Chen[8]

In the continental margin of the northeastern South China Sea, the sea level fluctuations since the Last Glacial Maximum have profoundly impacted the sedimentary environment. Our sub-bottom profiler data show a sedimentation process change from deposition to erosion during the Last Glacial Maximum. After the widespread erosion, the sedimentation process returned depositional throughout the Holocene, probably due to the rise of the sea level. This sedimentary process results in a widespread sedimentary unconformity in the continental slope, providing a benchmark for the end of the Last Glacial Maximum. Analyzing the sediment cores, we affirm that the change in current intensity is the primary factor controlling the sedimentary environments. The current intensities strengthened during the eustatic lowstand and weakened during the highstand periods, leading to alternating erosional and depositional processes. The widespread distribution of the erosive surface represents a regional-scale change in the sedimentary environment instead of a local event.

The global sea level change in the past 35,000 years may remarkably influence the sedimentary processes in the continental margin globally. The most important event of global climate change that occurred in that period was the Last Glacial Maximum (LGM), during which the global sea level dropped to a lowstand of about −120 to −134 m[1–5]. The sea level change could predominantly control the sedimentary environment of the continental margin especially in the continental shelf[6–8], because of the extremely coastline migration, changes in sediment supply, sea water temperature/salinity variation and current intensity changes. However, in the continental slope environment, sea level fluctuations may not affect sedimentary processes directly. The variation of contour current and contourite system could be more important factors in the sedimentary environment of the continental slopes.

Based on deep-tow sub-bottom profiler data, we have recognized an obvious sedimentary unconformity in the continental slope of the northeastern South China Sea (NE SCS), indicating sedimentation processes evolving from erosive to depositional on the seabed since the LGM. To understand the key factors that control the sedimentary process change and the relationship between paleoclimate and palaeoceanographic in the study area, we have also applied sediment core analysis and radiocarbon dating to depict the variation history of sediment facies, sedimentary environments, and ocean current intensities during different periods.

Regional setting

The study area is located in the continental margin of NE South China Sea, where the passive margin is in the west, and the active margin is in the east. (Fig. 1). Due to the eastward subduction of the Eurasian Plate beneath the Philippine Sea Plate, the Manila accretionary wedge of the active margin shows a series of pronounced bathymetric ridges and troughs[9–11]. As a result of substantial erosion of the Taiwan orogen, the Kao-Ping River and Erh-Jen River drainage areas have transported up to 79 Mt/yr of sediment discharge into the space off SW Taiwan[12]. Being the primary channels of sediment transportation from the continental shelf to the deep-sea basin, the Kaoping Canyon (KC) and the Penghu Channel (PC) mainly control the sedimentary environment off SW Taiwan or the northeastern margin of the South China Sea (Fig. 2a). However, those two canyon systems do not directly pass through our study area. According to previous studies[13–15], no obvious lateral evolution exists in the upper reach thalweg of the KC and PC. Thus, sediments in the study area are predominant hemipelagic and modulated by bottom or contour currents. Additionally, the gas hydrate could be widely

[1]Department of Earth Sciences, National Central University, Taoyuan, Taiwan. [2]Institute of Earth Sciences, Academia Sinica, Taipei, Taiwan. [3]Institute of Oceanography, National Taiwan University, Taipei, Taiwan. [4]Geo-Ocean,UMR6538, Univ-Brest, CNRS, Ifremer, 29280 Plouzané, France. [5]Université de Nice Sophia Antipolis, Nice, France. [6]Université de Montpellier, Géosciences Montpellier, CNRS, Montpellier, France. [7]Center for Environmental Studies, National Central University, Taoyuan, Taiwan. [8]Geological Survey and Mining Management Agency, Ministry of Economic Affairs, Taipei, Taiwan. ✉e-mail: hsu@ncu.edu.tw

Fig. 1 | The overview of the marine environment in the north South China Sea. The contour line of −134 m indicates the coastline in the LGM lowstand. It is noted that no water from the SCS has gone through the Taiwan Strait during the LGM lowstand. The black rectangle indicates the area of Fig. 2a. The thick red line shows the main stream and an intruded looping of Kuroshio Current[19]. The thick blue line shows the pathway of the Intermediate Water Circulation, modified from past studies[21–25]. The ADCP data in this study (heave blue arrow in the black rectangle). KC Kuroshio Current, IWC Intermediate Water Circulation, MT Manila Trench, RT Ryukyu Trench.
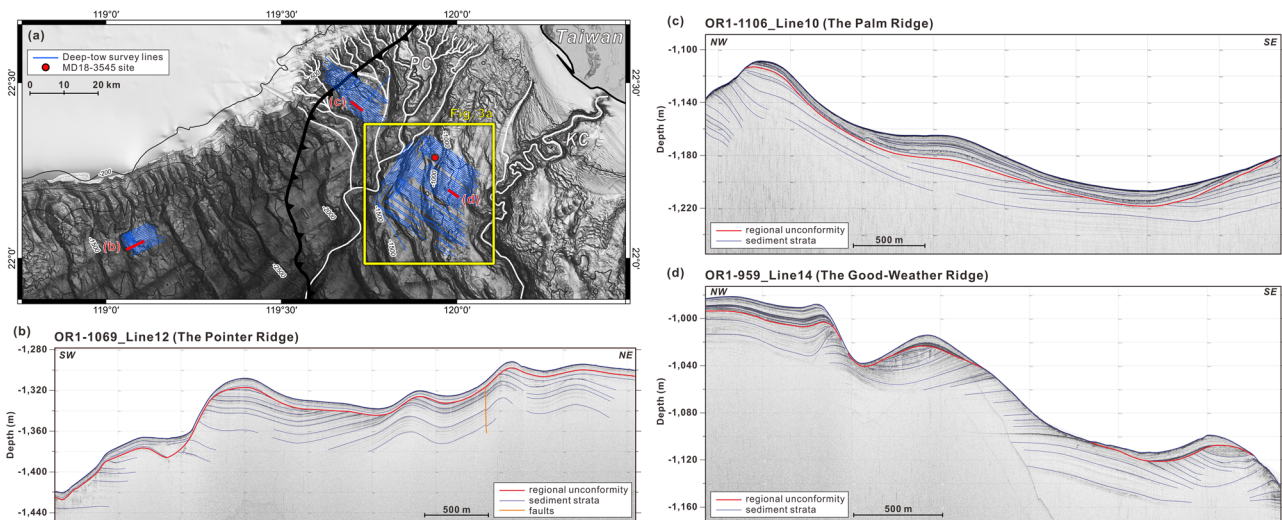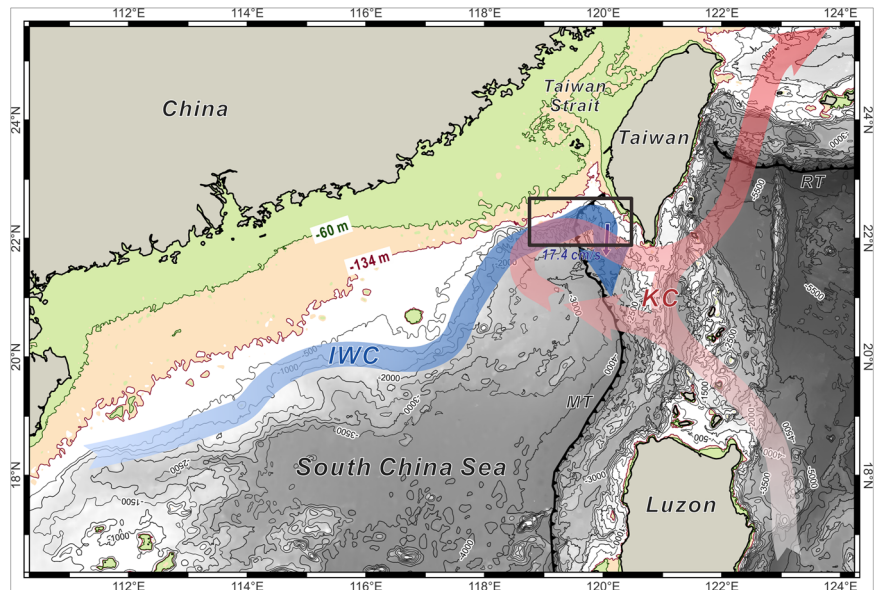

Fig. 2 | The sub-bottom profiler data and the regional unconformity in the continental slope of the NE South China Sea. a Blue lines indicate the deep-tow survey lines. A regional unconformity could be recognized in the continental slopes shown in the sub-bottom profiler (SBP) data of (**b**), (**c**) and (**d**). A red dot indicates the core site MD18-3545. The red line segments in (**a**) indicate the SBP locations of (**b**)–(**d**), which are the Pointer Ridge (**b**), the Palm Ridge (**c**), and the Good-Weather Ridge (**d**), respectively. PC Penghu Channel system, KC Kaoping Canyon system.

distributed off SW Taiwan; however, the related mud diaprism or gas emission out of seabed are generally located at water depths shallower than 600 m and do not affect the sediment distribution in our study area[16,17]. In contrast, contour currents play essential roles in the sedimentary process in the continental slopes globally[18]. In the northern South China Sea, several ocean currents could influence the marine environment of the continental margin. For instance, the seasonal intruded looping Kuroshio Current[19] has eroded the seabed and formed an erosional channel in the eastern shelf of the KC[20] (Fig. 1). As shown by seismic profiles and sediment cores, the clockwise circulated Intermediate Water Current (IWC) (Fig. 1) along the continental slope of the northern South China Sea (between −200 and −1200 m depth) has formed contourite systems[21–25]. In the western South China Sea, the IWC displays a speed between 5 and 15 cm/s and circulates between −750 and −1500 m deep[26,27]. Based on the stable isotope analysis results, the intrusion of the IWC from the Northern Pacific Ocean to the South China Sea has millennial-scale variations during the last deglaciation period, and the intrusion strength was related to surface water current and

winter moonsoon[28]. However, the relationship between the sea level change, bottom currents, and sedimentary processes in the NE South China Sea remains unknown.

Results and discussion
Regional unconformity
We have recognized a regional unconformity in the shallow sediments as shown in the SBP profiles (Figs. 2b–d and 3c). This regional unconformity separates two sedimentary sequences of different seismic facies. Beneath the unconformity, the seismic facies show numerous parallel reflectors with good continuity in the lower sequence. The regional unconformity has truncated the strata. On the other hand, the seismic facies show nearly homogeneous deposition above the unconformity. However, the upper sequence exhibits few reflectors showing strong and good continuity (Fig. 3c). The upper sequence shows a typical contourite system of drift and moat morphologies. The thickness of contourite drift or the sediments above the unconformity is varied but generally less than 50 meters (Fig. 3a).
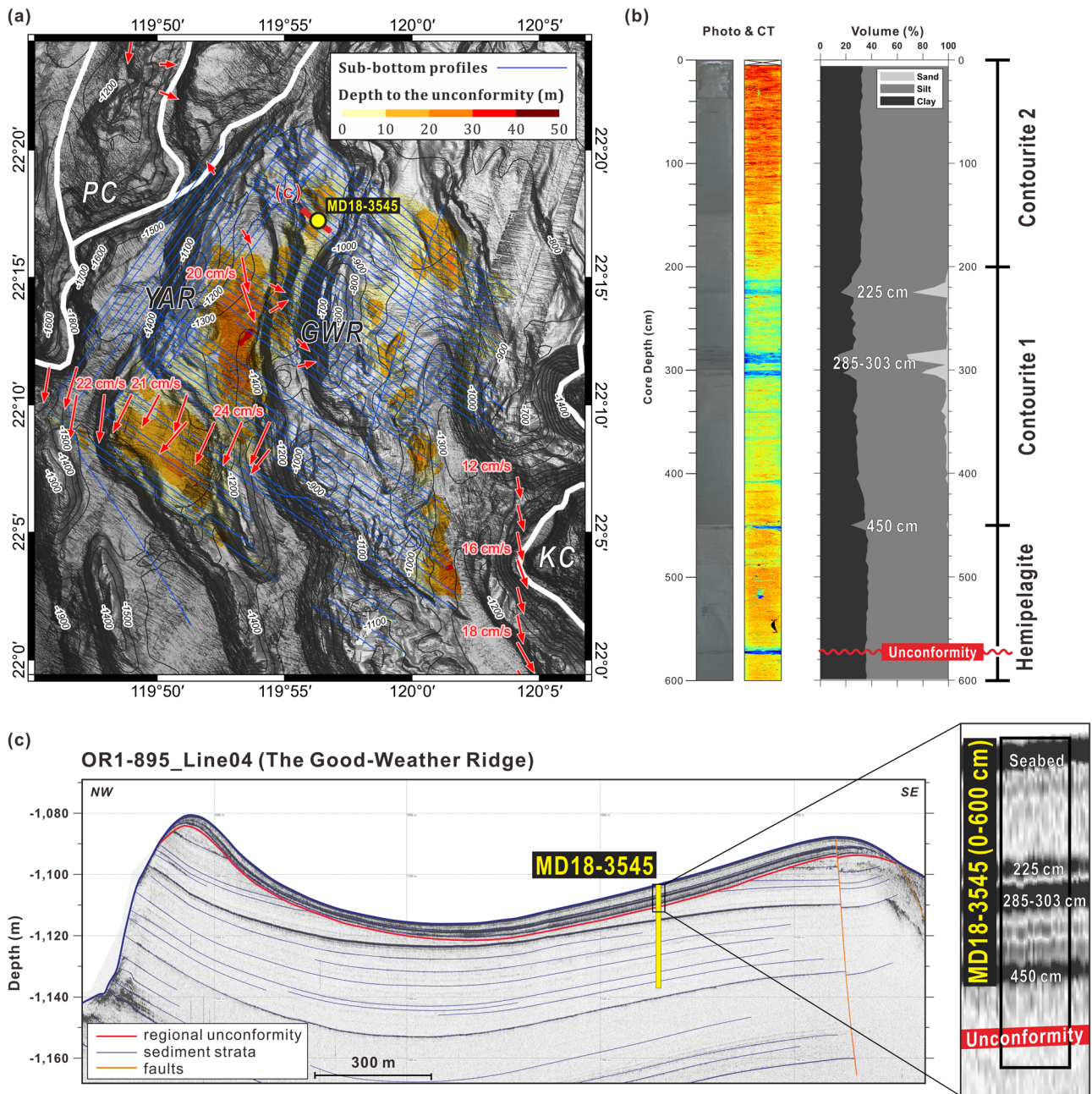
Fig. 3 | The regional unconformity around the Good-Weather Ridge (GWR) the Yung-An Ridge (YAR). a The color pattern shows the thickness of the sediments (or the contourite drifts) deposited on top of the unconformity. The contourite drifts are generally distributed on the relatively flat area, such as the flanks of the GWR or the terraces between ridges. The red arrows show the along-slope bottom current directions and velocities in the water depth between −1000 and −1200 m. **b** The core photo, CT image and sediment volumes of core MD18-3545. **c** The SBP profile across the site of core MD18-3545. In general, the strong reflectors in the SBP profile correspond to the layers of coarser sediments. KC Kaoping Canyon, PC Penghu Channel.

Due to the existence of the mass transport deposits (MTDs) in the strata above the regional unconformity to the west of the GWR, the sediment thickness in the west is much thicker than that in the east of the GWR (Fig. 3a and Supplementary Fig. 2). The contourite drifts are located on the relatively flat areas such as both flanks of the GWR and terraces between ridges (Fig. 3a). Some steep bathymetric ridges show erosive features without sediment deposition, indicating local strong contour currents (Figs. 2c, d and 3c).

Radiocarbon dating

The result of the radiocarbon datings is shown in Supplementary Table 1 and Fig. 4. In general, the core is younger upward (Supplementary Fig. 3), except for the sample at core depth 310 cm, where a reworking process from

regional event may have deposited some coarser and older sediments (Fig. 4). Remarkably, a sedimentary hiatus is found between the samples at core depth 470 cm and core depth 590 cm (i.e., between 9300 and 35,547 cal yr BP) (Fig. 4). The hiatus corresponds to the regional unconformity at core depth 575 cm, covering the period of the LGM (Fig. 5).

Sediment core characteristics and PSA results

The sediment core MD18-3545 is located in the northwestern area of the GWR (Fig. 3a). We have analyzed the top 600 cm of the core, containing the sediments above the unconformity and the uppermost sediments beneath the unconformity (Fig. 3c). The texture of the deposits shows homogeneous, silt rich properties in the core description and photos. The regional unconformity is situated at a depth of 575 cm with a showing an erosive
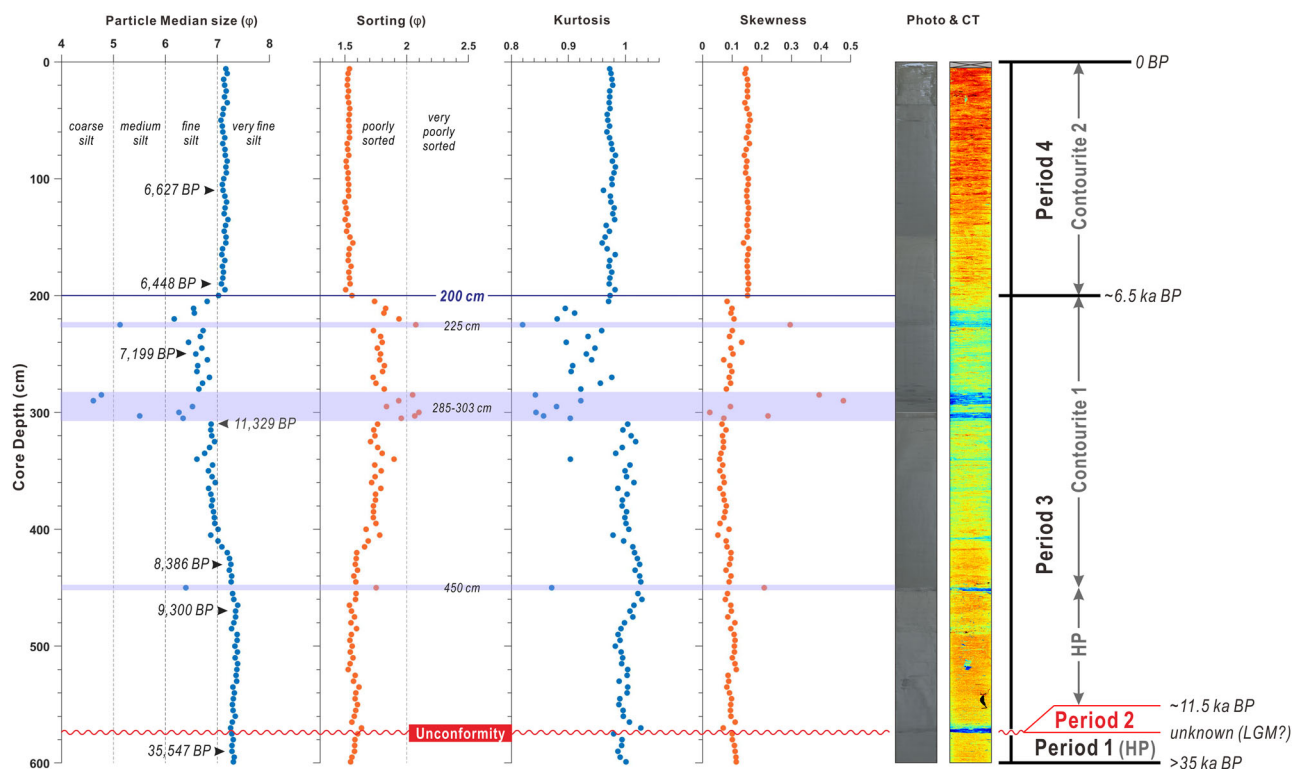
Fig. 4 | The analysis results of the top 600 cm of core MD18-3545. The charts from left to right are particle median size, sorting, kurtosis, skewness, core photo and CT image, respectively. Based on the core analysis results, we could distinguish four sedimentary periods and sediment facies in each period. The black arrows with age numbers indicate the radiocarbon dating depths and calibrated results (in median). The light purple stripes indicate the layers of coarser sediments in the core segment. HP Hemipelagite.

contact at the base and a fining-upward trend (Fig. 3b and Supplementary Fig. 1). Although the texture is relatively homogeneous in the core segment, we still can distinguish some differences from the PSA results and CT images, and separate the core into four sedimentary periods (Fig. 4). The definition of sedimentary periods correlates with the SBP profiles' seismic facies. In an ascending order, the four sedimentary periods are (Fig. 4):

Period 1 (P1): From core depth 575 to 600 cm (~35.5 cal ka BP), it is a depositional period with stable grain size characteristics (Fig. 4). Sediments pertain to very fine silts and are poorly sorted with intense bioturbation showing no clear physical sedimentary structures (Supplementary Fig. 1). These sedimentary characteristics and sediment facies are consistent with the nature of hemipelagite.

Period 2 (P2): At the core depth of 575 cm (ages roughly correspond from LGM to ~11.5 cal ka BP), an erosional interface separates the depositional Period 1 and Period 3. The photo and CT images of the core show a sharp erosional surface on top of Period 1 deposits (Supplementary Fig. 1). This erosional interface indicates an erosional period between Period 1 and Period 3. The PSA results show no apparent particle size change before and after this period, but the sorting, kurtosis and skewness have slightly offset after this unconformity (Fig. 4).

Due to the lack of sediments during Period 2, which is erosive in nature, we do not know the exact starting age of the erosion. However, the sample dating beneath the unconformity shows that the erosional process started after 35.5 cal ka BP (Fig. 4). The exact starting age of the regional erosion could be later, because some strata beneath the bathymetric ridge to the southeast of core MD18-3545 and beneath the unconformity reveal that the erosional process must be younger than 35.5 ka BP (Fig. 3c). On the other hand, the samples above the unconformity show that the erosional process ceased at about 11.5 cal ka BP (Fig. 4).

Period 3 (P3): From core depth 575 to 200 cm (~11.5 cal ka to ~6.5 cal ka BP), the environment returned to a depositional setting. The particle sizes show coarsening-upward trend, grading from very fine to fine silts.

The degree of sorting increase with increasing particle sizes, and the kurtosis and skewness also fluctuate in this segment (Fig. 4). According to the PSA and core images, we divide this core section into two subsections. The subsection from core depth 575 to 450 cm is similar to Period 1, showing hemipelagic facies with stable very fine silt content and rich in bioturbation (Fig. 4 & Supplementary Fig. 1). In the subsection from core depth 450 to 200 cm, the PSA results show a coarsening-upward trend in particle size (Fig. 4). It shows less of bioturbation with scattered few foraminifera and shell fragments (Supplementary Fig. 1). Although the photo of the core shows a homogeneous texture, we observe laminated structures in this subsection. To understand which sediment type of this subsection, we refer to different typical fine-grained sedimentation facies models in the continental margin, including fine-grained turbidite, silty/muddy contourite and hemipelagite[29]. Moreover, this subsection exhibits contourite facies instead of hemipelagic facies in the previous subsection, which has slightly grain size change, indistinct laminated structures (Supplementary Fig. 1). There are several submarine canyons (e.g., KC and PC) around the study area. However, their distances or sediment pathways are far from the core site. The elevation difference is large from the core site to the thalweg of the canyons. Moreover, the sediment facies does not show typical features of fine-grained turbidites such as sharp basal contact, upward fining grading in grain size, sandy base layer, good sorting and poor bioturbation[29,30]. We therefore exclude the possibility that the sediments are laid down by turbidity currents. Several coarser layers at core depths 225 cm, 285 cm, 290 cm, 303 cm, and 450 cm, respectively, have different sediment characteristics, which contain much higher sand volume (>20%), poorer sorting, lower kurtosis and higher skewness values (Figs. 3b and 4). These coarser layers correspond to the reflections featuring strong and good continuity in the SBP profiles (Fig. 3c). The origin of these particularly coarser layers may be due to the regionally individual events.

Period 4 (P4): From core depth 200 to 0 cm (~6.5 cal ka BP to present), particle sizes remain very stable in the range of very fine silt. The sorting,
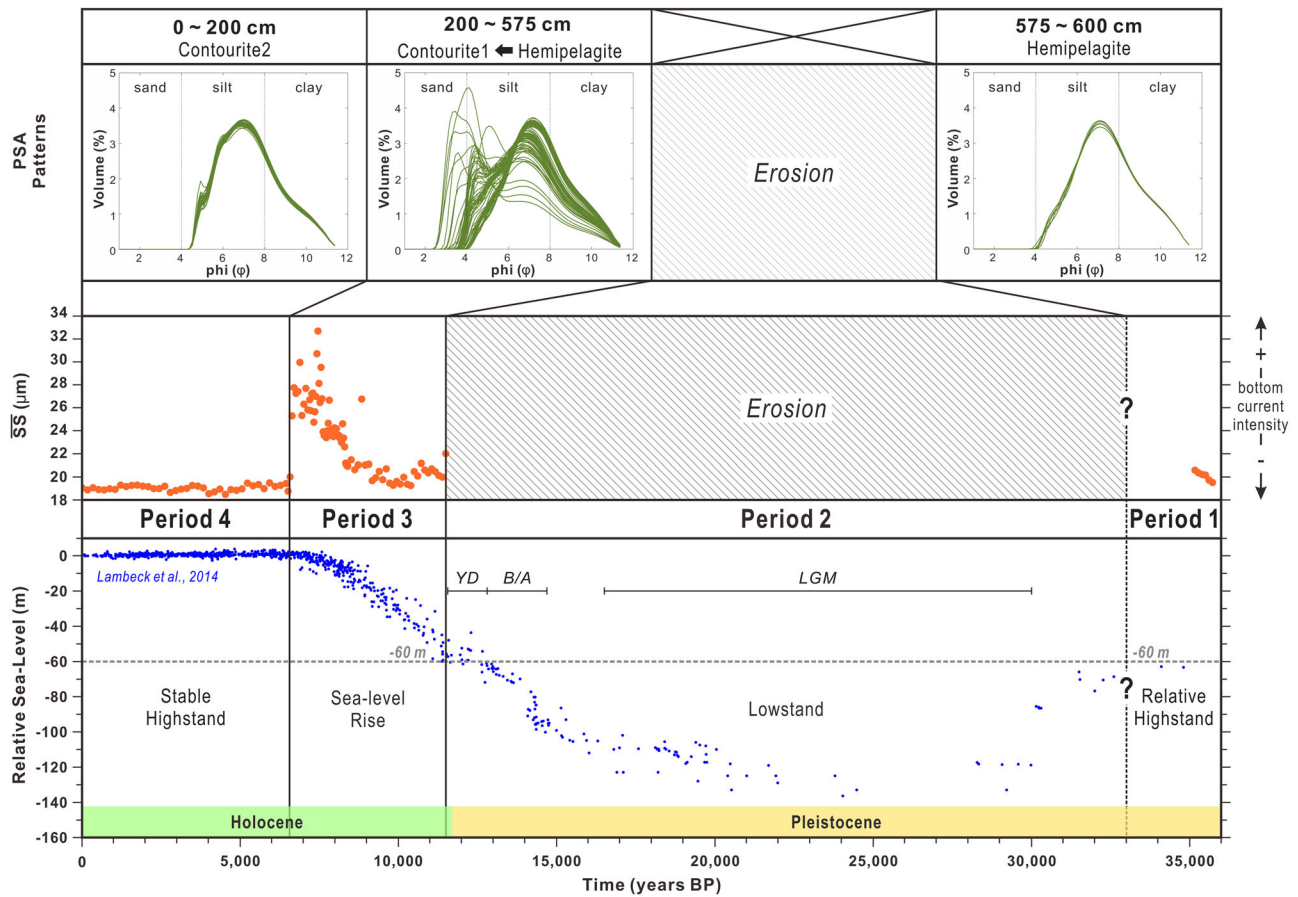
Fig. 5 | The PSA patterns, mean sortable size $\overline{SS}$ and sea level fluctuations since 35,000 BP. (Top) The PSA patterns of the depositional periods P1, P3 and P4. Each pattern shows different sedimentary facies. (middle) The sortable silt mean size ($\overline{SS}$) of MD18-3545, which responds to the bottom current intensity during sedimentation. (bottom) The global sea level change in the past 35,000 yr[5]. Generally, a bottom current intensity is positively correlated to the gradient of the sea level change. The strong erosion in Period 2 occurred at a lowstand of the sea level or at water depths lower than about −60 m. The depositional Periods 3 and 4 occurred when the sea level is higher than −60 m. B/A Bølling–Allerød, YD Younger Dryas.

---

kurtosis and skewness of the sediments are also relatively homogeneous (Fig. 4). Whereas, compared to the previous period (P3), there are noticeable changes in texture, including finer particle size, lower sorting, lower kurtosis and higher skewness (Fig. 4). Clear laminated structures can be found in the CT images (Supplementary Fig. 1). A few foraminifera and shell fragments are shown in core descriptions. The above features suggest that this core section is consistent with a contourite facies.

The present state of bottom currents
The ADCP data in the water depth from −1000 to −1200 m show a consistent along-slope current direction (Fig. 3a). The average azimuth of the currents is about 183°. The mean current speed is about 17.4 cm/s (Supplementary Fig. 4), similar to the IWC speed (5 to 15 cm/s) observed in the western SCS[26,27]. The ADCP data were collected from 3 cruises in different seasons, and the current shows the same direction and velocity during these cruises. We do not see any spatial variations in the current intensity in the study area. Therefore, we consider the bottom current consistent and not influenced by other down-slope flows, such as turbidity currents. The currents are coherent with the clockwise circulated IWC in the northern margin of the South China Sea[21-25] (Fig. 1). The IWC could be the essential role in forming the NE South China Sea contourite system.

Variation of ocean bottom current intensity
In the continental margin, the bottom current intensity is one of the major factors controlling the grain sizes of sediments. In general, bottom current intensities are proportional to mean silt sizes on the seafloor[31,32]. Taking into account the cohesive behavior of fine-grained sediments in the 2 to 10 μm size range, the mean size of the non-cohesive sortable silt (10 to 63 μm) is controlled by bottom current speed[33-36]. Powerful bottom currents may resuspend the unconsolidated seafloor sediments, selectively eroding the finer components or re-depositing the coarser ones. The mean sizes of the sortable silt ($\overline{SS}$) of core MD18-3545 in Period 1 are relatively fine as shown in Fig.5. After the erosional Period 2, the $\overline{SS}$ of the first subsection (from 11.5 to 8.8 cal ka BP) of Period 3 is similar. Then, the $\overline{SS}$ size in the second subsection (from 8.8 to 6.5 cal ka BP) of Period 3 has increased positively. After Period 3, the $\overline{SS}$ size abruptly drops to a relatively fine size in Period 4. The depositional Period 1 and Period 4 have relatively slower bottom current intensities according to the proportional relationship between bottom current intensities and the sortable silt mean sizes. The erosion of sediments in Period 2 suggests an occurrence of stronger bottom current intensities, causing the widespread erosional feature that leads to the regional unconformity. However, in Period 3, the depositional process resumed, though the bottom current intensities could be even stronger. The reason that the sedimentary environment changed from erosional to deposition in Period 3 under the same or even higher bottom current intensities is probably due to the rise of the relative sea level to −60 m in Period 3 (Fig. 5). In other words, the rise of sea level or the increase of seawater pressure on the seafloor may strengthen fine sediments against erosion from bottom currents.

Sea level and sedimentary environment
Compared our core analysis results to the global sea level change since 35 ka BP[5], we find that the variation of the sedimentary environment is highly

related to the sea level change (Fig. 5). The eustatic variation has led to the difference in the bottom current intensity, then the sedimentary environment. Depositional periods 1, 3 and 4 took place during the sea level highstands or deglacial stages, while the erosional Period 2 occurred during the lowstand (LGM) (Fig. 5). In general, when the relative sea level is lower than −60 m, an erosion of the seafloor appears in our study region (Fig. 5). In Period 3, the sea level rises rapidly, and the sedimentary environment changes from erosional to depositional. The deglaciation arrived in the final phase at the beginning of Period 4 (~ 6.5 cal ka BP), when the rapid rise in sea levels stopped. After that, the sea level has remained relatively stable range.

Each sedimentary period exhibits a different sea level status and a different sediment facies pattern. During the Period 1, the PSA chart of volumes (%) in each particle size displays a symmetrical and unimodal pattern (Fig. 5). The sediment's characteristics present a typically hemipelagic facies, indicating weak or non-existent of bottom currents.

During Period 2, the global lowstand greatly limited the distribution of sea water of the NE South China Sea. The Taiwan Strait was exposed entirely because of the lowered sea level (Fig. 1). The limited water body could have changed the water temperature and salinity that increased the bottom current intensity in the continental margin of NE South China Sea. The strong current switched the sedimentary process from depositional to erosive and caused the regional erosional surface (i.e., the unconformity). The increase of the bottom current intensities during cold periods was also reported in the margins of the Gulf of Cadiz[37] and the Northern Tyrrhenian Sea[38]. An additional factor that enhanced the seabed erosion during the eustatic lowstand could be the seabed instability caused by more methane emitted from the seabed[39,40]. The erosive environment of the continental slope could also affect the cold seep system in the NE South China Sea[41,42]. After the LGM, most coastlines in the NE South China Sea retreated significantly due to the rapid rise of the sea level (Fig. 1). Sea water started intruding from the North Pacific into the SCS through Luzon Strait in the deglacial stage. The intruded current strength varied with winter monsoon strength in different global climate intervals (Heinrich 1, Bølling-Allerød and Younger Dryas)[28].

During Period 3, the relative sea level steeply rose from about −60 to 0 m. The frequency of turbidity currents in the KC also significantly increased when the climate became more humid and warmer off SW Taiwan than in the previous period[43]. However, due to the location and morphology of the study area, turbidity currents did not accumulate sediments in the study area and formed turbidites. In the core MD18-3545, the $\overline{SS}$ distribution indicates a prevalence of strong bottom currents in Period 3 (Fig. 5). The patterns of the PSA charts also show a change from unimodal to coarser-sized bimodal in Period 3, indicating that the sedimentary environment has affected by gradually increasing bottom currents (Fig. 5). Moreover, the sediment characteristics and the sedimentary features in the CT images change from hemipelagic to contourite facies (Fig. 5). In general, a change of the sedimentary environment from erosion to deposition is mainly due to a decrease of bottom current intensity. Thus, the sediments would have been eroded in Period 3 instead of a depositional period. A depositional environment in Period 3 could be due to the rise of sea levels (Fig. 5), which increases the resistance of sediments from erosion.

During Period 4, a stable sea level and weak bottom currents provide a rather stable environment for sediment deposition, when the seawater area of the NE South China Sea reaches its maximum coverage (Fig. 1). We compare the shoreline distances during stages of sea-level lowstand (P2), sea-level rising (P3) and sea-level highstand (P4) periods, the main sediment source during P4 should be predominant from Taiwan as other periods may be sourced from both Taiwan and southeastern China (Fig. 1). Therefore, the change in sea level influenced both current intensity and sediment source during this period. Although the bottom current intensity is weak in Period 4, the bottom current still plays a vital role in the sedimentation. We observe features of contourite drift from SBP profiles in Period 4 and the contourite features seems to persist until the present-day. The PSA chart shows coherently partial bimodal patterns in Period 4 (Fig. 5), indicating

the weak winnowing process[25,33,34,44–46] caused by bottom currents on the seabed environment.

Considering the PSA results, radiocarbon dating and sea level records, we conclude that the rate of sea level change influences the bottom current intensities. Both the relative sea level changes and the bottom currents control the sedimentation processes in the continental margin of the NE South China Sea.

Conclusions

We identify a widespread unconformity in the continental slope of the NE South China Sea using deep-towed high-resolution sub-bottom profiler data. The marine environment has dramatically varied due to the change in relative sea level and bottom current intensity. The sedimentary hiatus occurred during the LGM and Younger Dryas stage (from 35.5 to 11.5 cal ka BP), when strong bottom currents took place during a lowstand stage of sea level, and the current erosion caused the regional unconformity. The regional unconformity in the NE South China Sea can be treated as a sequence boundary to distinguish the pre-LGM strata from the post-LGM successions. The sedimentary environment resumed as depositional in the Holocene when the relative sea level was above −60 m. We reconstruct the history of changes in bottom current intensity since 35 ka BP based on the analysis of the sediment particle sizes and radiocarbon dating results. The bottom current intensity change reflects the IWC's history of sea level changes in the late Quaternary. The depositional Period 3 (11.5 to 6.5 cal ka BP) and Period 4 (6.5 cal ka BP to present) occurred during rapid sea level rise and stable sea level, respectively. As the relative sea level gradually increased in Period 3, the intensity of the bottom current also gradually increased. A regional contourite sequence occurred in Period 3. Although the sea level has ceased the rapid rising tendency and the bottom current intensity becomes relatively low in Period 4, a weak winnowing process and contourite system are still ongoing. In the continental margin of the NE South China Sea, the sea level change has affected the bottom current intensities, the sedimentary processes, the seafloor morphologies, and the cold seep systems in the last 35 ka.

Data and Method
Sub-Bottom Profiler (SBP)
To understand the high-resolution seabed structures, we used the Edgetech 2400 deep-towed high-resolution sonar system. The towed fish was deployed at about 40 m about the seafloor, which can provide a vertical resolution of the SBP data of 15–25 cm in the frequency band of 1.5–6 kHz. We can have a vertical SBP image up to 60 m deep, depending on the seabed roughness and near-surface sediment types. Overall, 60 survey lines were conducted during 5 different cruises from 2008 to 2013 (Fig. 2a). Every survey line was laid back to the accurate position by using the GPS data of the vessel, the towed cable length and the bathymetric data acquired from the vessel and the towed fish. The SBP data were processed, interpreted, and outputted by SonarWiz software. Time-variant gain and AGC were applied to enhance the image quality. The y-axis in the SBP profiles is depth in meters, converted from two-way travel time by giving a seawater and sediment sound velocity of 1500 m s^{-1} and 1600 m s^{-1}, respectively.

Sediment core
To understand the nature of the regional unconformity and the relationship of the sediment characteristics with the SBP images, a giant Calypso piston core MD18-3545, which penetrated the regional unconformity, was acquired in the northwestern flank of the Good-Weather Ridge (GWR) in the MD214/EAGER cruise by R/V Marion Dufresne[47] (Fig. 2a). The water depth of the coring site is 1136 m and the recovered core is 33.88 m. The scientific party on board carried out the core description and photography. Each core segment was split into two halves for working and archive purposes. The working half was subsequently used for sampling and analyses. The archived half was stored and was analyzed by CT (Computed Tomography) scanning at Taiwan Instrument Research Institute (TIRI).

Particle size analysis (PSA)

To analyze the sediment grain sizes, 121 samples were taken from the top 600 cm of core MD18-3545 with a spacing of 5 cm. Each sample is 1 cm in thickness. The sample treatment and measurement works were conducted in the Sediment Analysis Lab of National Central University. To avoid the influences of organic matters and biological shells on the results of the PSA, the sample treatments followed the procedure suggested in ISO 11277[48], which included drying the samples with a freeze dryer, removing organic matter with 15% hydrogen peroxide (H_2O_2) and removing carbonates with 10% hydrochloric acid (HCl). The PSA was performed by a Beckman Coulter LS13 320 laser diffraction particle size analyzer. For each sample, the measurement result shows each size's volume percentages, and several sediment characteristics were calculated, including mean size, median size, mode, sorting, skewness, and kurtosis.

Radiocarbon dating

AMS ^{14}C dating was applied to constrain the age of the top 600 cm of core MD18-3545. Overall, four species of planktonic foraminifera were picked from 7 depth segments of the core (Supplementary Table 1), and all the samples were cleaned with methanol (CH_3OH) and sodium hypochlorite (NaOCl) to remove the organic matters attached to the tests. After that, the samples were sent to NTUAMS Lab for dating. The results of ^{14}C ages were calibrated by the Calib 8.2 radiocarbon calibration web service[49] with MARINE20 calibration curve[50]. Due to the lack of regional reservoir ΔR data around the study area in the MARINE20 database, we assume the ΔR to be 550 years.

Acoustic Doppler Current Profiler (ADCP)

The ADCP data were collected during the cruises LGD2010 (Oct. to Nov. 2020), LGD2108 (Sep. to Oct. 2021), and LGD2205 (Jun. 2022) by R/V Legend. Using the hull-mounted Teledyne Ocean Surveyor 38 kHz ADCP, we can detect current velocities and directions in the water deeper than 1000 meters. This study processed ADCP data with the CASCADE V7.2 software, including data cleaning, tide correction, and filtering. Considering the study area's water depth of target features, we select the bottom current velocities between 1000 and 1200 meters for the study.

Data availability

The particle size analysis data that support the findings of this study have been deposited in "figshare" website: https://doi.org/10.6084/m9.figshare.26200190.v2[51].

References

1. Fairbanks, R. G. A 17,000-year glacio-eustatic sea level record: influence of glacial melting rates on the Younger Dryas event and deep-ocean circulation. *Nature* **342**, 637–642 (1989).
2. Rohling, E. J. et al. Magnitudes of sea-level lowstands of the past 500,000 years. *Nature* **394**, 162–165 (1998).
3. Siddall, M. et al. Sea-level fluctuations during the last glacial cycle. *Nature* **423**, 853–858 (2003).
4. Clark, P. U. et al. The last glacial maximum. *Science* **325**, 710–714 (2009).
5. Lambeck, K., Rouby, H., Purcell, A., Sun, Y. & Sambridge, M. Sea level and global ice volumes from the Last Glacial Maximum to the Holocene. *PNAS* **111**, 15296–15303 (2014).
6. Vail, P. R., Mitchum Jr., R. M. & Thompson III, S. in *Seismic Stratigraphy — Applications to Hydrocarbon Exploration* Vol. 26 (ed Charles E. P.) 63–81 (American Association of Petroleum Geologists, 1977).
7. Wagoner, J. C.V. et al. in *Sea-Level Changes: An Integrated Approach* Vol. 42 (eds Cheryl K. W. et al.) 39–45 (SEPM Society for Sedimentary Geology, 1988).
8. Wagoner, J. C. V., Mitchum, R. M., Campion, K. M. & Rahmanian, V. D. Siliciclastic sequence stratigraphy in well logs, cores, and outcrops: concepts for high-resolution correlation of time and facies. *AAPG Meth. Exploration Ser.* https://doi.org/10.1306/Mth7510 (1990).
9. Liu, C.-S., Deffontaines, B., Lu, C.-Y. & Lallemand, S. Deformation patterns of an accretionary wedge in the transition zone from subduction to collision offshore southwestern Taiwan. *Mar. Geophys. Researches* **25**, 123–137 (2004).
10. Lin, A. T. et al. Tectonic features associated with the overriding of an accretionary wedge on top of a rifted continental margin: An example from Taiwan. *Mar. Geol.* **255**, 186–203 (2008).
11. Lin, A. T., Yao, B., Hsu, S.-K., Liu, C.-S. & Huang, C.-Y. Tectonic features of the incipient arc-continent collision zone of Taiwan: Implications for seismicity. *Tectonophysics* **479**, 28–42 (2009).
12. Dadson, S. J. et al. Links between erosion, runoff variability and seismicity in the Taiwan orogen. *Nature* **426**, 648–651 (2003).
13. Chen, G.-Y. Structures, Physiography and Development of The Penghu Submarine Canyon Off Southwest Taiwan. Master Thesis. National Central Univ. (2005).
14. Chiang, C.-S. & Yu, H.-S. Morphotectonics and incision of the Kaoping submarine canyon, SW Taiwan orogenic wedge. *Geomorphology* **80**, 199–213 (2006).
15. Chiang, C. & Yu, H. Sedimentary erosive processes and sediment dispersal in Kaoping submarine canyon. *Sci. China Earth Sci.* **54**, 259–271 (2010).
16. Hsu, S.-K. et al. Turbidity Currents, Submarine Landslides and the 2006 Pingtung Earthquake off SW Taiwan. *Terrestrial, Atmosph. Oceanic Sci.* https://doi.org/10.3319/tao.2008.19.6.767 (2008).
17. Chen, S.-C. et al. Distribution and characters of the mud diapirs and mud volcanoes off southwest Taiwan. *J. Asian Earth Sci.* **92**, 201–214 (2014).
18. Hernández-Molina, F. J., Llave, E. & Stow, D. A. V. in *Contourites* (*Developments in Sedimentology*, Volume 60) (eds M. Rebesco & A. Camerlenghi) Ch. 19, 379–408. Elsevier (2008).
19. Nan, F., Xue, H. & Yu, F. Kuroshio intrusion into the South China Sea: A review. *Prog. Oceanogr.* **137**, 314–333 (2015).
20. Yeh, Y.-C. et al. Continental shelf morphology controlled by bottom currents, mud diapirism, and submarine slumping to the east of the Gaoping Canyon, off SW Taiwan. *Geo-Marine Lett.* https://doi.org/10.1007/s00367-020-00673-5 (2021).
21. Lüdmann, T., Wong, H. K. & Berglar, K. Upward flow of North Pacific Deep Water in the northern South China Sea as deduced from the occurrence of drift sediments. *Geophys. Res. Lett.* https://doi.org/10.1029/2004gl021967 (2005).
22. Li, H. et al. Seismic characteristics and processes of the Plio-Quaternary unidirectionally migrating channels and contourites in the northern slope of the South China Sea. *Mar. Pet. Geol.* **43**, 370–380 (2013).
23. Chen, H. et al. Depositional characteristics and processes of alongslope currents related to a seamount on the northwestern margin of the Northwest Sub-Basin, South China Sea. *Mar. Geol.* **355**, 36–53 (2014).
24. Gong, C. et al. The northeastern South China Sea margin created by the combined action of down-slope and along-slope processes: Processes, products and implications for exploration and paleoceanography. *Mar. Pet. Geol.* **64**, 233–249 (2015).
25. Wang, X. et al. Controls of contour currents on intra-canyon mixed sedimentary processes: Insights from the Pearl River Canyon, northern South China Sea. *Mar. Geol.* **406**, 193–213 (2018).
26. Quan, Q., Xue, H., Qin, H., Zeng, X. & Peng, S. Features and variability of the South China Sea western boundary current from 1992 to 2011. *Ocean Dyn.* **66**, 795–810 (2016).
27. Yin, S. et al. Isolation of the South China Sea from the North Pacific Subtropical Gyre since the latest Miocene due to formation of the Luzon Strait. *Sci. Rep.* **11**, 1562 (2021).

28. Yang, Y., Xiang, R., Zhong, F. & Wan, S. The variability of Intermediate water intrusion into the South China Sea during the last deglaciation. *Palaeogeogr. Palaeoclimatol. Palaeoecol.* https://doi.org/10.1016/j.palaeo.2024.112127 (2024).

29. Stow, D. & Smillie, Z. Distinguishing between deep-water sediment facies: turbidites, contourites and hemipelagites. *Geosciences* **10**, 68 (2020).

30. Stow, D. A. V. & Faugères, J.-C. in *Contourites (Developments in Sedimentology, Volume 60)* (eds M. Rebesco & A. Camerlenghi) Ch. 13, 223–255 (Elsevier, 2008).

31. Ledbetter, M. T. A Late Pleistocene time-series of bottom-current speed in the Vema Channel. *Palaeogeogr., Palaeoclimatol., Palaeoecol.* **53**, 97–105 (1986).

32. Ledbetter, M. T. Bottom-current pathways in the Argentine Basin revealed by mean silt particle size. *Nature* **321**, 423–425 (1986).

33. McCave, I. N., Manighetti, B. & Beveridge, N. A. S. Circulation in the glacial North Atlantic inferred from grain-size measurements. *Nature* **374**, 149–152 (1995).

34. McCave, I. N., Manighetti, B. & Robinson, G. Sortable silt and fine sediment size/composition slicing: Parameters for palaeocurrent speed and palaeoceanography. *Paleoceanography* **10**, 593–610 (1995).

35. McCave, I. N., Crowhurst, S. J., Kuhn, G., Hillenbrand, C. D. & Meredith, M. P. Minimal change in Antarctic Circumpolar Current flow speed between the last glacial and Holocene. *Nat. Geosci.* **7**, 113–116 (2013).

36. McCave, I. N., Thornalley, D. J. R. & Hall, I. R. Relation of sortable silt grain-size to deep-sea current speeds: Calibration of the 'Mud Current Meter. *Deep Sea Res. Part I: Oceanographic Res. Pap.* **127**, 1–12 (2017).

37. Llave, E. et al. High-resolution stratigraphy of the Mediterranean outflow contourite system in the Gulf of Cadiz during the late Pleistocene: The impact of Heinrich events. *Mar. Geol.* **227**, 241–262 (2006).

38. Miramontes, E. et al. The Pianosa Contourite Depositional System (Northern Tyrrhenian Sea): Drift morphology and Plio-Quaternary stratigraphic evolution. *Mar. Geol.* **378**, 20–42 (2016).

39. Hsu, S.-K. et al. Tide-modulated gas emissions and tremors off SW Taiwan. *Earth Planet. Sci. Lett.* **369-370**, 98–107 (2013).

40. Hsu, S.-K. et al. Seabed gas emissions and submarine landslides off SW Taiwan. *Terrestrial, Atmos. Ocean. Sci.* **29**, 7–15 (2018).

41. Feng, D. et al. Cold seep systems in the South China Sea: An overview. *J. Asian Earth Sci.* **168**, 3–16 (2018).

42. Kuo, M.-Y. et al. New records of three deep-sea bathymodiolus mussels (bivalvia: mytilida: mytilidae) from hydrothermal vent and cold seeps in Taiwan. *J. Mar. Sci. Technol.* **27**, 352–358 (2019).

43. Yu, S.-W. et al. Sea level and climatic controls on turbidite occurrence for the past 26 kyr on the flank of the Gaoping Canyon off SW Taiwan. *Mar. Geol.* **392**, 140–150 (2017).

44. Faugères, J.-C. & Mulder, T. in *Developments in Sedimentology* Vol. 63 (eds H. HüNeke & T. Mulder) Ch. 3, 149–214 (Elsevier, 2011).

45. Mulder, T. et al. Contourites in the Gulf of Cadiz: a cautionary note on potentially ambiguous indicators of bottom current velocity. *Geo-Mar. Lett.* **33**, 357–367 (2013).

46. de Castro, S. *et al*. Contourite characterization and its discrimination from other deep-water deposits in the Gulf of Cadiz contourite depositional system. *Sedimentology* https://doi.org/10.1111/sed.12813 (2020).

47. Nathalie, B. & Gueorgui, R. MD 214 / EAGER cruise, RV Marion Dufresne. https://doi.org/10.17600/18000520 (2018).

48. ISO-11277. in *Soil quality - Determination of particle size distribution in mineral soil material - Method by sieving and sedimentation* (International Organization for Standardization, 2020).

49. Stuiver, M., Reimer, P. J. & Reimer, R. W. *CALIB 8.2*, (2021).

50. Heaton, T. J. et al. Marine20—The Marine Radiocarbon Age Calibration Curve (0–55,000 cal BP). *Radiocarbon* **62**, 779–820 (2020).

51. Chen, K.-T. (figshare, 2024).

Author contributions
Conceptualization: K.-T. Chen. and S.-K. Hsu. Investigation: S.-K. Hsu, A. T.-S. Lin, C.-C. Su, N. Babonneau, G. Ratzov, S. Lallemand, P.-C. Huang, L.-K. Lin, H.-S. Lin, C.-H. Tsai and S.-C. Chen. Methodology: K.-T. Chen, S.-K. Hsu and A. T.-S. Lin. Data Analyses: K.-T. Chen. Writing: K.-T. Chen. and S.-K. Hsu. Discussion and Review: S.-K. Hsu, A. T.-S. Lin, N. Babonneau, S. Lallemand and J.-Y. Lin.

Competing interests
The authors declare no competing interests.

Additional information
Supplementary information The online version contains supplementary material available at https://doi.org/10.1038/s43247-024-01593-3.

Correspondence and requests for materials should be addressed to Shu-Kun Hsu.

Peer review information *Communications Earth & Environment* thanks Huang Haibo, Haiteng Zhuo and the other, anonymous, reviewer(s) for their contribution to the peer review of this work. Primary Handling Editor: Carolina Ortiz Guerrero. A peer review file is available.

Reprints and permissions information is available at http://www.nature.com/reprints

Publisher's note Springer Nature remains neutral with regard to jurisdictional claims in published maps and institutional affiliations.